Dalton Transactions

ROYAL SOCIETY OF CHEMISTRY

PAPER

View Article Online
View Journal | View Issue

Cite this: *Dalton Trans.*, 2024, **53**, 13044

Photosubstitution and photoreduction of a diazido platinum(IV) anticancer complex†

Huayun Shi, ‡[a] Christian Ward-Deitrich, ‡[b] Fortuna Ponte, [c] Emilia Sicilia, *[c] Heidi Goenaga-Infante *[b] and Peter J. Sadler *[a]

Received 30th May 2024,
Accepted 11th July 2024

DOI: 10.1039/d4dt01587h

rsc.li/dalton

The hyphenation of HPLC with its high separation ability and ICP-MS with its excellent sensitivity, allows the analysis of Pt drugs in biological samples at the low nanomolar concentration levels. On the other hand, LC-MS provides molecular structural confirmation for each species. Using a combination of these methods, we have investigated the speciation of the photoactive anticancer complex diazido Pt(IV) complex *trans*, *trans*, *trans*-[$Pt(N_3)_2(OH)_2(py)_2$] (**FM-190**) in aqueous solution and biofluids at single-digit nanomolar concentrations before and after irradiation. **FM-190** displays high stability in human blood plasma in the dark at 37 °C. Interestingly, the polyhydroxido species [{$Pt^{IV}(py)_2(OH)_4$} + Na]$^+$ and [{$Pt^{IV}(py)_2(N_3)(OH)_3$} + Na]$^+$ resulting from the replacement of azido ligands, as determined by LC-MS, were the major products after photoirradiation of **FM-190** with blue light (463 nm). This finding suggests that such photosubstituted Pt(IV) tri- and tetra-hydroxido species could play important roles in the biological activity of this anticancer complex. Density Functional Theory (DFT) and Time-Dependent DFT (TDDFT) calculations show that these Pt(IV) species arising from **FM-190** in aqueous media can be formed directly from a singlet excited state. The results highlight how speciation analysis (metallomics) can shed light on photoactivation pathways for **FM-190** and formation of potential excited-state pharmacophores. The ability to detect and identify photoproducts at physiologically-relevant concentrations in cells and tissues will be important for preclinical development studies of this class of photoactivatable platinum drugs.

1. Introduction

Platinum drugs have been widely used in chemotherapy since the FDA approval of cisplatin for testicular cancer treatment in 1978.[1,2] Owing to the lack of selectivity and dose-limiting side effects of cisplatin, photoactive Pt(IV) complexes that are more kinetically stable are being developed as a new generation of platinum drugs.[3–7] Photoactive Pt(IV) complexes offer the prospect of low toxicity towards normal tissue, and selective cytotoxicity towards tumours when irradiated with spatially-directed light.[8–13] Octahedral diam(m)ine dihydroxido diazido Pt(IV) complexes are especially promising for further development. They display a significant stability in the dark under physiological conditions and photocytotoxicity towards a wide range of human cancer cells.[5,6] *cis*,*trans*,*cis*-[$Pt(N_3)_2(OH)_2(NH_3)_2$] was the first reported photoactive anticancer diazido Pt(IV) complex.[14] However, the all-*trans* analogue *trans*,*trans*,*trans*-[$Pt(N_3)_2(OH)_2(NH_3)_2$] exhibits improved aqueous solubility, a more intense and *ca.* 30 nm red-shifted LMCT band, and an enhanced photocytotoxicity.[15–17] Replacement of an ammine ligand with pyridine results in *trans*,*trans*,*trans*-[$Pt(N_3)_2(OH)_2(NH_3)(py)$] with high UVA photocytotoxicity.[18] Notably, compared with photolabile ammine ligands, no pyridine release is detected upon irradiation. *trans*,*trans*,*trans*-[$Pt(N_3)_2(OH)_2(py)_2$] (**FM-190**, Fig. 1a) with two pyridine ligands has a promising visible light photocytotoxicity.[19]

The photoactivation of **FM-190** in aqueous solution has been investigated previously to provide insights into its mechanism of action.[19,20] Pt(II) species and azidyl radicals appear to be the main cytotoxic species produced by such photoactivated diazido Pt(IV) complexes.[5] Pt(II) species can bind to DNA and azidyl radicals can attack proteins.[5] The formation of Pt(II) species has been monitored by NMR, UV-vis, LC-MS, Attenuated Total Reflection Fourier Transform Infrared (ATR-FTIR) spectroscopy, and transient electronic absorption (TEA) spectroscopy.[19,20] In addition, photo-substitution of one azide ligand by a H_2O/OH molecule has been frequently reported as an initial step in the photoactivation of diazido

[a]*Department of Chemistry, University of Warwick, Coventry CV4 7AL, UK. E-mail: P.J.Sadler@warwick.ac.uk*
[b]*LGC Limited, National Measurement Laboratory (NML), Queens Road, Teddington, Middlesex TW11 0LY, UK. E-mail: heidi.goenaga-infante@lgcgroup.com*
[c]*Department of Chemistry and Chemical Technologies, University of Calabria, via Pietro Bucci, 87036 Arcavacata di Rende, Cs, Italy. E-mail: emilia.sicilia@unical.it*

†Electronic supplementary information (ESI) available. See DOI: https://doi.org/10.1039/d4dt01587h

‡These authors contributed equally.

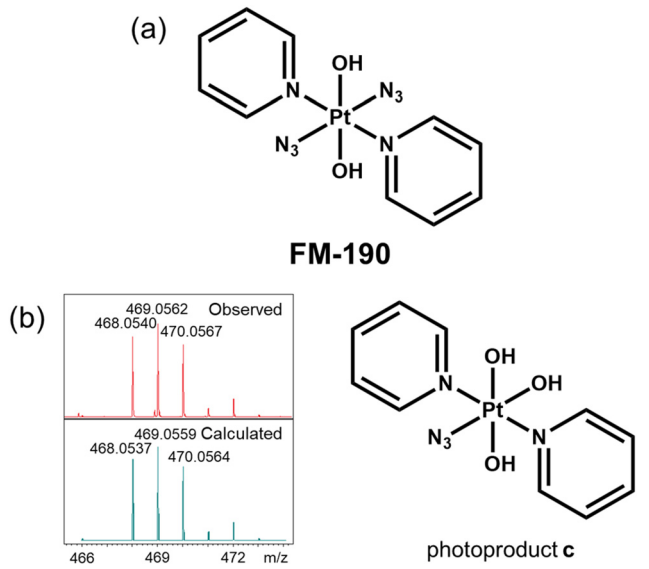

Fig. 1 (a) Structure of photoactivatable Pt(IV) complex **FM-190** studied in this work. (b) HR-MS and expected structure of the main photoproduct **c** ($[\{Pt^{IV}(py)_2(N_3)(OH)_3\} + Na]^+$, *m/z* 469.0562) from **FM-190** in water.

Pt(IV) complexes.[5,6] However, due to the sensitivity limit, accurate qualitative and quantitative analysis of Pt(II) and Pt(IV) species at nanomolar concentrations, which is important for *in vivo* investigations, cannot be achieved using these methods. DFT calculations can also help to elucidate possible photodecompostion pathways.

Due to its high selectivity, mass spectrometry based on characteristic mass-to-charge ratios (*m/z*) of analytes and their fragments is used for a wide range of applications.[21–23] Inductively coupled plasma-mass spectrometry (ICP-MS) has received intense attention in the development of metal-based drugs as a standalone configuration or coupled to separation techniques, and can be applied in the determination of not only extracellular transformations of metallodrugs, but also their accumulation, distribution, and processing in cells, tissues and organs.[24–27] Reverse phase high performance liquid chromatography (RP-HPLC) is a most frequently used separation technique, due to its promising capability for separating a wide range of compounds.[28,29] The combination of HPLC and ICP-MS provides the potential for the accurate analysis of the products from interaction of metallodrugs with small biomolecules,[30] their binding to proteins by (metallo)-proteomics,[31,32] as well as the dark stability and metabolism of metallodrugs in human plasma and cells at nanomolar concentrations.[26,33–35]

Investigations of classical platinum drugs using HPLC-ICP-MS have been widely reported, including their stability in biofluids, interactions with biomolecules, and adducts within cells, but photoactive diazido Pt(IV) complexes have not yet been fully explored.[36–45] Here, we have developed an HPLC-ICP-MS method for Pt analysis at extremely low, physiologically-relevant concentrations, and used HPLC-MS and ESI-HR-MS to identify the speciation of **FM-190** in aqueous solution, phosphate-buffered saline (PBS) and human blood plasma in the dark and upon irradiation. We have also optimised the extraction methods for photoproducts of **FM-190** in plasma. DFT calculations were carried out to investigate possible mechanisms of photoactivation based on the photoproducts detected by mass spectrometry. This work provides a foundation for the accurate speciation analysis of photoactive Pt(IV) complexes in body fluids, cells and tissues.

2. Results

2.1. HPLC-ICP-MS method development

To achieve reliable quantification of Pt species at biologically relevant nanomolar levels, a detector with high sensitivity and selectivity, such as ICP-MS, is required to be hyphenated to HPLC. HPLC-UV methods were explored as summarised in Table S1,† and the corresponding chromatograms are shown in Fig. S1.† Method-7 was selected as the best choice to reduce the amount of carbon entering ICP-MS, at the same time allowing **FM-190** to be eluted from the column. It was then applied in all HPLC-ICP-MS experiments. Using method-7, a linear relationship between concentration and peak area was observed for **FM-190** for the concentration range of 0.06 to 17.6 μM with r^2 = 0.999 (Fig. S2†). However, when the concentration was lower than 60 nM, no HPLC-UV peak was visible.

FM-190 (764.8 nM) prepared in water was injected onto the C18 column, and the separated Pt species sequentially detected by the ICP-MS detector. For the dark samples (Table S2†), a peak at 14.1 min was detected and assigned as **FM-190** with purity of 99. 9% (Table S3†). The slight shift in retention time (0.2 min) for the HPLC-ICP-MS is caused by the difference in distance between UV and ICP-MS detectors and the HPLC column (Fig. 2a). Three Pt isotopes (^{194}Pt, ^{195}Pt, and ^{196}Pt) were measured, and similar results were observed for all of them, with signals matching the abundance of these isotopes (Fig. S3†). This experiment was independently repeated twice to ensure the reproducibility of the method. If not stated otherwise, the ^{195}Pt signal from the first repetition is used to represent the result obtained for HPLC-ICP-MS in this paper. **FM-190** at lower concentrations of 45.9, 9.2, and 4.6 nM were also measured using the same method (Fig. 2b–d, Table S3†). A single main Pt-peak with the same retention time was detected for all of the samples, highlighting the high sensitivity for detection of ICP-MS, down to low nM concentrations. A linear relationship between concentrations and sum of ^{195}Pt peak areas is observed (Fig. 2e). Notably, the two very small peaks at 4.6 (0.065%) and 8.8 (0.048%) min were only detectable when the **FM-190** concentration was 764.8 nM, but not at lower concentration levels (Table S3†).

2.2. Photoactivation of FM-190 in water determined by HPLC-ICP-MS

The Pt-containing photoactivation products were also determined by HPLC-ICP-MS. However, to ensure no retention of side products on the C18 column, method-8 was adopted by

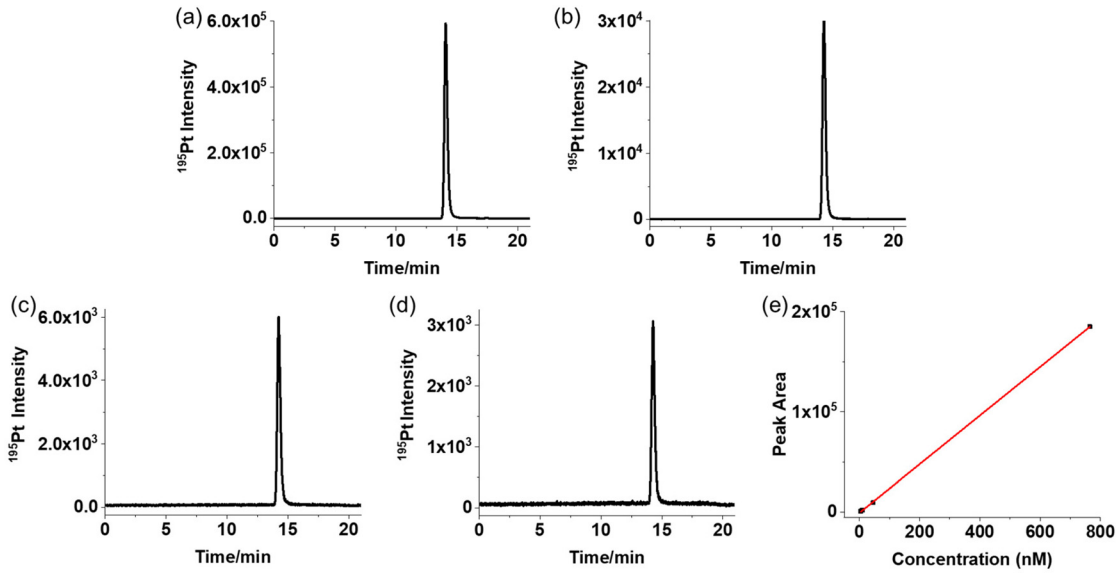

Fig. 2 ^{195}Pt signals of **FM-190** in MilliQ water in the dark obtained by HPLC-ICP-MS at (a) 764.8; (b) 45.9; (c) 9.2; and (d) 4.6 nM; and (e) the relationship between the concentration of **FM-190** and sum of peak areas of ^{195}Pt signals.

adding a column washing step (Table S2†). A total of 8 Pt-containing ICP-MS peaks were detected for **FM-190** (764.8 nM) in water after 1 h irradiation with blue light (463 nm, Fig. 3a and Table S4†). An approximate 92% decrease in the peak area assigned to **FM-190** was observed. These species are stable in solution for 24 h in the dark at 25 °C (Fig. 3b). Notably, when the concentration of **FM-190** was decreased to 45.9 and 4.6 nM, only 5 Pt species were detected after irradiation (Fig. 3c–d and Table S4†). Notably, when the concentration of **FM-190** was 4.6 nM, the smallest peak detected in the irradiated sample had a concentration of *ca.* 0.16 nM. A linear relationship was found between the Pt concentration and the sum of all peak areas in all samples, suggesting all Pt containing species are determined, and that quantification of Pt using HPLC-ICP-MS is also reliable for photoactivated samples (Fig. 3e).

2.3. Photoactivation of FM-190 in water investigated by LC-MS

In order to identify the species formed from **FM-190** in aqueous solution upon irradiation with blue light (463 nm,

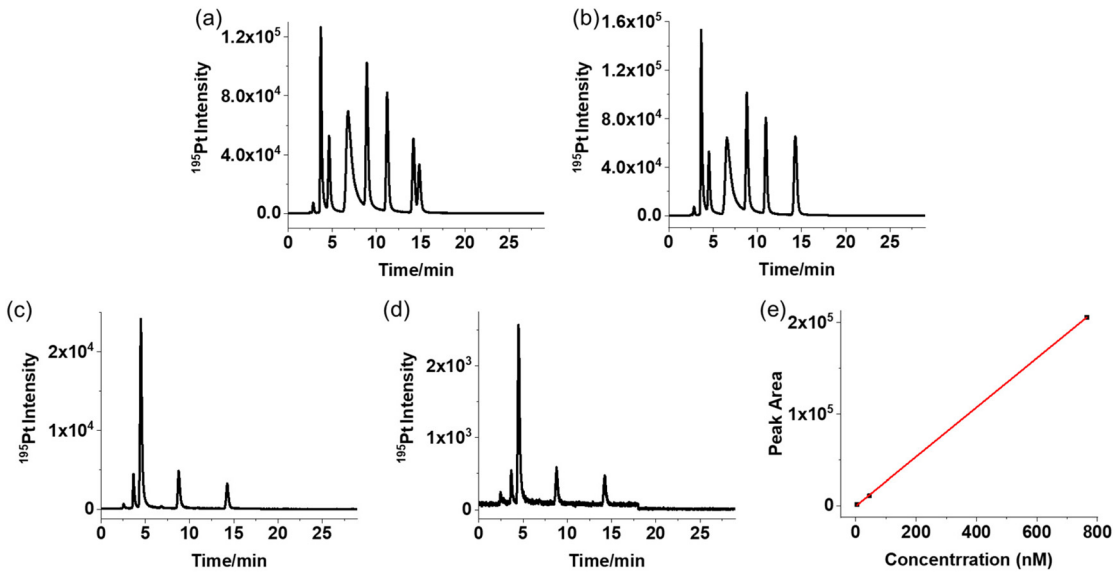

Fig. 3 ^{195}Pt signals of **FM-190** in MilliQ water after irradiation with blue light (463 nm, 1 h) obtained by HPLC-ICP-MS at (a) 764.8 nM determined immediately, and (b) after samples had stood for 24 h in the dark; (c) 45.9; and (d) 4.6 nM; and (e) the relationship between concentration of **FM-190** and sum of peak areas of ^{195}Pt signals.

1 h, 25 °C), LC-MS was used. For LC-MS, the same methods as those used in HPLC-ICP-MS, method-7 (2% to 5% B in 10 min, maintain 5% B for 5 min) and method-8 (80% B after 18 min), were used for dark and irradiated samples, respectively, to ensure all species were detected (Table S2†). After 1 h irradiation with blue light (463 nm), 6 main species were observed for photoactivated **FM-190** (31.8 μM) solutions (Fig. S4†). The retention times of these species are similar to those detected in HPLC-ICP-MS. The detection of more species by HPLC-ICP-MS compared with LC-MS suggests a lower detection limit of the HPLC-ICP-MS method. In addition, the difference in peak intensities between HPLC-ICP-MS and LC-MS arises from the varied ability of these species to form molecular ions. The peak at 13.9 min is assigned to **FM-190** itself. Photoproducts are assigned as $[\{Pt^{IV}(py)_2(OH)_4\} + Na]^+$ (*m*/*z* 443.95, **a**); $[\{Pt^{IV}(py)_2(OH)_3\}_2(\mu\text{-}O_2) + Na]^+$ (*m*/*z* 863.04, **b**); $[\{Pt^{IV}(py)_2(N_3)(OH)_3\} + Na]^+$ (*m*/*z* 468.95, **c**); $[\{Pt^{III}(py)_2(HCOO)(OH)_2(H_2O)\} + Na]^+$ (*m*/*z* 472.94, **d**); and $[\{Pt^{II}(py)_2(HCOO)_3\} + H]^+$ (*m*/*z* 488.94, **e**), summarised in Table S5.† Species $\{Pt^{III}(py)_2(OH)_2\}^+$ (*m*/*z* 386.96) was observed in all peaks, and might be formed during ionisation by release of the corresponding ligands. The isotopic pattern for platinum was observed in all species (Fig. S5†). Notably, the most abundant photoproduct (**c**) found by LC-MS can be assigned as $[\{Pt^{IV}(py)_2(N_3)(OH)_3\} + Na]^+$, which is a Pt(IV) species from photo-substitution rather than a Pt(II) species resulting from photoreduction. The fraction containing the main Pt(IV) species **c** was collected to obtain high resolution MS data, determined to be 469.0562 and matches well with calculated value of 469.0559 (Fig. 1b). These results also suggest that the photoproducts remained stable after lyophilisation. Unfortunately, attempts to purify species **c** were unsuccessful, perhaps due to its reactivity under the conditions used. For 1.3 μM **FM-190**, only two photoproducts were detected due to the low sensitivity of the LC-MS method compared with HPLC-ICP-MS (Fig. S4c and S6c†). Interestingly, the **FM-190** LC-MS peak disappeared after irradiation at this low concentration (1.3 μM), while being still visible when the concentration was higher (31.8 and 6.4 μM).

In order to exclude the effect of mobile phases, water and acetonitrile with 0.1% formic acid (FA) were also used as the mobile phases. This is the most common mobile phase combination used in LC-MS for the study on Pt species.[5] However, mobile phase composition needs to be evaluated since there is possibility that acetonitrile can become a potential binding partner and an acidic pH can result in ligand release. Similar species with different retention times were determined for photoactivated **FM-190** at concentrations of 50 μM using method-10, where acetonitrile was used instead of methanol as mobile phase B (Fig. S7, Tables S6 and S7†). This suggests that the organic mobile phase exerts no significant effects on the detection of these photoproducts.

2.4. DFT calculations

2.4.1. Simulated absorption spectra of FM-190 in water. DFT calculations were carried out to investigate the detailed mechanism of photoactivation based on the photoproducts detected by LC-MS. To describe the photophysical properties of **FM-190**, a preliminary benchmark study was carried out on its absorption spectrum in water. Several exchange and correlation functionals were explored (Table S8†). Hybrid B3LYP functional can simulate the electronic spectrum appropriately, and was therefore employed for the complete characterisation of **FM-190**. The calculated absorption spectrum is in very good agreement with the reported experimental spectrum (Fig. S8†).[19] Both spectra show two absorption bands in the UV region. The most intense band arising from several electronic transitions, is centred at 300 nm ($f = 0.3610$). Notably, the first singlet excited state S1, dark in nature, falls at 478 nm in the blue region of the visible spectrum and corresponds to a charge transfer from the Highest Occupied Molecular Orbital (HOMO) to the Lowest Unoccupied one (LUMO). TDDFT calculations assign the bright singlet state to the transition at 394 nm originating from a H−2 → L MOs transition. The second band that falls in the 250–280 nm spectral range is characterised by transitions with different features (Table S9†). It is centred at 262 nm and the theoretical assignment for the most important transitions show that it is a mixed band with Ligand-to-Ligand (LLCT) and Ligand-to-Metal (LMCT) characters.

2.4.2. Excited states properties and photoactivation mechanism of FM-190 in water. Population of electronically-excited states is important for the PACT activity of **FM-190**. A detailed TDDFT analysis of the excited states was conducted, aiming at investigating its behaviour under photoexcitation. In order to elucidate the reaction pathways for irradiated **FM-190** involving promotion of efficient intersystem crossing (ISC) from the bright state (S3) or low-lying singlet states (S1–S2) to the low-lying triplet states (T1–T5), the spin–orbit matrix elements and the adiabatic energy difference between the singlet and triplet states were calculated. Excitation energies, absorption wavelength, molecular orbital (MO) contribution and theoretical assignment for S1–S3 singlet states and T1–T5 triplet states are reported in Tables S10 and S11,† while spin-orbit coupling (SOC) values are provided in Table S12.† Natural transition orbital (NTO) plots for singlet and triplet states are depicted in Fig. S9 and S10,† respectively. The data reported in Table S12† can be rationalized in the framework of El-Sayed rules[46] stating that a significant enhancement in SOC can be produced if the radiationless transition involves an orbital type change. In this case, the highest SOC values are calculated for states involving different kinds of charge transfer. The most effective couplings correspond to S1 → T1, S2 → T1, S2 → T3, S3 → T2 and S3 → T5 transitions.

Once the feasibility of ISC processes was established, for the accurate characterization of the involved triplet excited states, their structures were optimized using the TDDFT approximation. Indeed, as singlet excited states generally have a lifetime five orders of magnitude shorter than that of triplet states (10^{-8} *vs.* 10^{-3} s), it is reasonable to assume that the primary mechanism for the formation of Pt(II) active species involves an excited triplet state rather than a singlet state. As a consequence, the optimized structures obtained for the triplet

		S0	Ta	Tb	Tc	Td
a) Optimised structure		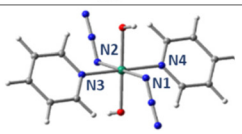	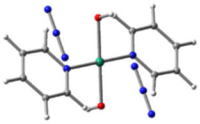	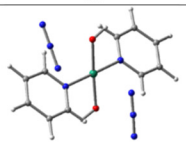	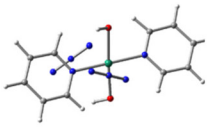	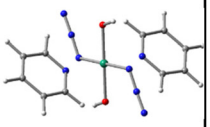
Bond Length (Å)		Pt-N1=2.0994 Pt-N2=2.0994 Pt-N3=2.0768 Pt-N4=2.0768	Pt-N1=2.3416 Pt-N2=2.3416 Pt-N3=2.0943 Pt-N4=2.0943	Pt-N1=2.5116 Pt-N2=2.6857 Pt-N3=2.0814 Pt-N4=2.0784	Pt-N1=2.5062 Pt-N2=2.6356 Pt-N3=2.0808 Pt-N4=2.0761	Pt-N1=2.1213 Pt-N2=2.1213 Pt-N3=2.4047 Pt-N4=2.4047
b) Plot of spin density distribution			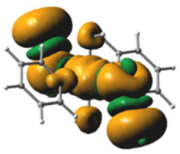	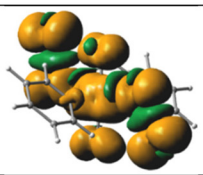	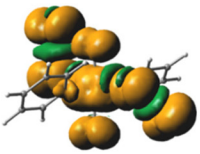	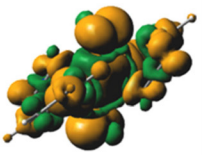
c) Spin density values (SD in a.u.)	Pt		0.541	0.589	0.613	0.923
	N1		0.321	0.237	0.247	0.025
	N2		0.427	0.314	0.317	0.028
	N3		0.321	0.282	0.286	0.025
	N4		0.427	0.346	0.349	0.028
d) ΔE(eV)			1.60	1.51	1.45	1.81

Fig. 4 (a) Structures of the optimised S0 ground state and Ta, Tb, Tc and Td triplet states together with relevant bond lengths (in Å) compared with corresponding GS values. (b) Plot of spin density distribution. (c) Spin density values (SD in a.u.) for Pt and nitrogen atoms directly bonded to the metal centre. (d) Relative energies calculated with respect to the GS.

states, served as initial points for the optimization within the unrestricted Kohn–Sham formalism (UKS),[47,48] known to mitigate instabilities in excited triplet states involving charge transfer. Applying this approach, all the examined triplet excited states collapsed into four distinct states denoted as Ta, Tb, Tc, and Td. Detailed information about the obtained triplet states, namely optimized structures together with the corresponding spin density distributions, spin density values on the Pt centre and N atoms directly bonded to the metal, relative energies calculated with respect to the ground state (GS) and the main bond distances are provided in Fig. 4.

As is evident, Ta, Tb, and Tc triplet structures exhibit dissociative character towards both azide ligands, while the py ligands remain firmly attached to the Pt centre. However, Td triplet shows two elongated Pt–py bonds, while azides remain in the Pt coordination sphere. This particular triplet state is considered unlikely, since no pyridine release from **FM-190** was observed experimentally, and thus excluded from the investigation of photoreaction. The relative energies of the excited triplet states calculated respect to the ground state follow the order Tc < Tb < Ta < Td. As the optimised geometries of the most stable Tc and Tb triplets indicate that such states are highly dissociative for the N_3 ligands, with the Pt–N_3 distances significantly elongated by 0.5 Å (Pt–N1) and 0.6 Å (Pt–N2) compared to the ground-state geometry, they give rise to the formation of the $[Pt^{II}(OH)_2(py)_2]$ photoproduct. In the Ta triplet state, however, the Pt–N_3 bonds are partially elongated and the distance increases by approximately 0.3 Å. Generally, an excited state exhibiting MC character cannot be involved in the emissive processes, but it can play a role as an

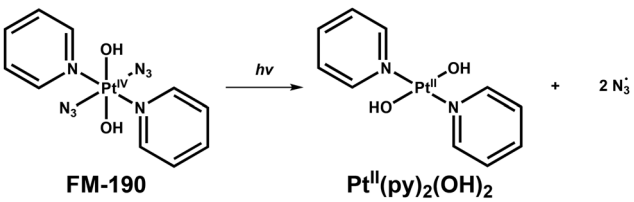

Scheme 1 Proposed photoreduction mechanism for the formation of the Pt(II) product based on DFT calculations.

active species in the release of reactive ligands.[49] In this context, the nature of all the intercepted triplet states (^{3}MC) promote ligand photodissociation. Based on these results, formation of photoproducts from **FM-190** can be achieved by following two paths. First, the population of Tb and Tc states leads to the formation of the reduced form, $[Pt^{II}(OH)_2(py)_2]$, of **FM-190** as shown in Scheme 1. Second, the Ta triplet state could lead to the formation of the aquated forms of the complex. Experimental data show that **FM-190** is inert until it is converted to active aquated forms, through the release of N_3 ligands. Starting from the Ta state, all the attempts to identify minima and transition states along triplet pathways leading to the formation of mono-aquated and/or bi-aquated species failed. Therefore, it is realistic to postulate that from the complex in its excited triplet state only the reduced photoproduct $[Pt^{II}(OH)_2(py)_2]$ can be generated as a result of the elimination of the two $N_3^{\bullet}$ radicals.

On the contrary, formation of Pt(IV) products, experimentally detected by MS and obtained by substitution of

anionic N_3^- ligands with water molecules, might take place from **FM-190** in its singlet ground state, but only when overcoming high energy barriers according to calculations. Further explorations are required to completely reconcile experimental and theoretical results, although probing the possible involvement of excited singlet states will require use of more sophisticated computational strategies.

According to computational analysis, reaction intermediates $[Pt^{IV}(N_3)(H_2O)(OH)_2(py)_2]^+$, $[Pt^{IV}(H_2O)(OH)_3(py)_2]^+$ and the final product $[Pt^{IV}(OH)_4(py)_2]$ are generated along pathways in singlet multiplicity. The proposed mechanism leading to the formation of the intermediates and the final product is shown in Scheme 2, and the calculated energy profile for this process is shown in Fig. 5. Relative energies are calculated with respect to the reference energy of the first formed adduct between **FM-190** and two water molecules set as the zero on the energy scale.

According to the proposed mechanism, the first hydrolysis process for the Pt complex occurs following a second-order nucleophilic substitution. One of the N_3^- ligands is displaced from **FM-190** in favor of the coordination of a water molecule, leading to the formation of the intermediate $[Pt^{IV}(N_3)(H_2O)(OH)_2(py)_2]^+$ that lies 9.6 kcal mol^{-1} above the reference energy of the corresponding first adduct. The mono-aquated Pt(IV) complex $[Pt^{IV}(N_3)(H_2O)(OH)_2(py)_2]^+$ is formed by overcoming an energy barrier of 35.6 kcal mol^{-1}. Starting from intermediate $[Pt^{IV}(N_3)(H_2O)(OH)_2(py)_2]^+$, the reaction can proceed by both deprotonation of the bound water molecule and replacement of the second azide ligand by water. In the former case, overcoming a very low energy barrier, only 1.1 kcal mol^{-1}, allows the formation of the $[Pt^{IV}(N_3)(OH)_3(py)_2]$ species, that is calculated to be endergonic by 8.1 kcal mol^{-1} with respect to reference zero energy of the first adduct is achieved.

The second N_3^- ligand is replaced with the same mechanism by a second molecule of water, but during the course of the reaction, the transfer of a proton from the coordinated water molecule to the N_3^- ligand detached in the first step occurs simultaneously. The height of the barrier that is necessary to overcome for such a rearrangement to occur is 35.2 kcal mol^{-1}, while the second $[Pt^{IV}(H_2O)(OH)_3(py)_2]^+$ intermediate is destabilised with respect to the initial adduct by 16.0 kcal mol^{-1}. Both kinetics and thermodynamics significantly favor the deprotonation reaction according to experimental findings that assign $[\{Pt^{IV}(py)_2(N_3)(OH)_3\}+Na]^+$ (**c**) as the main product. Finally, the Pt(IV) species $[Pt^{IV}(OH)_4(py)_2]$ (**a**) is formed through the protonation of the N_3^- group present in the reaction environment by the coordinated water molecule. The formation of final product is calculated to be endergonic by

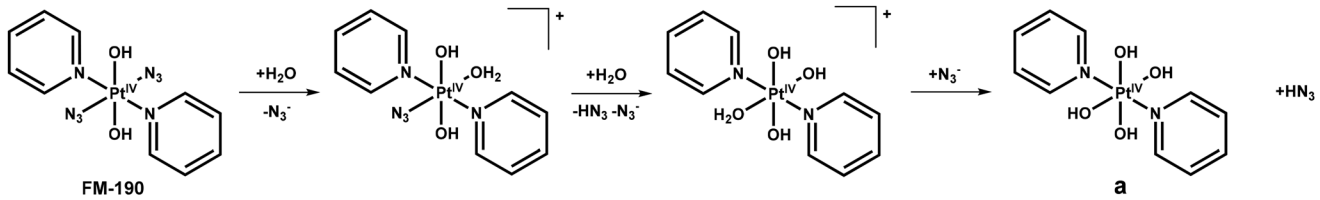

Scheme 2 Proposed mechanism for the formation of hydrolysed Pt(IV) products based on DFT calculations.

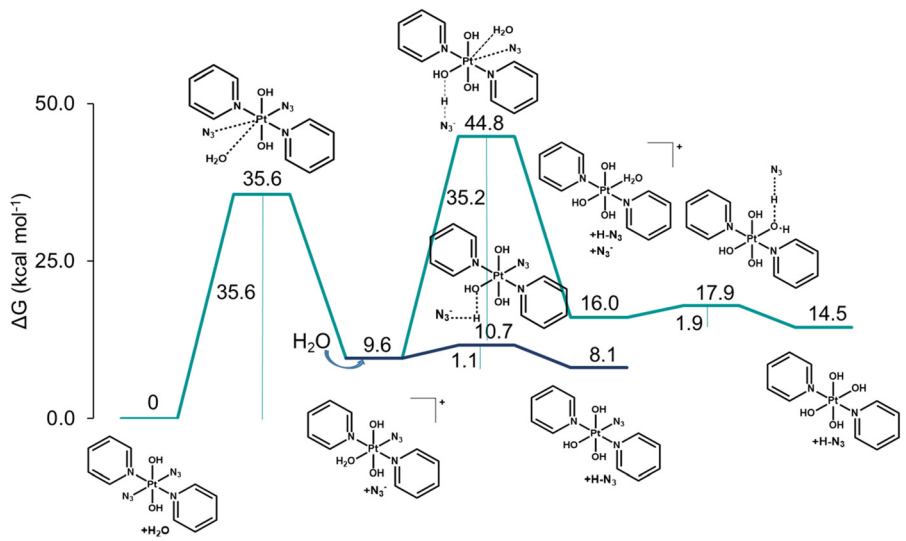

Fig. 5 DFT-calculated free energy profile in water describing the hydrolysis mechanism of **FM-190**. Relative energies are in kcal mol^{-1} and calculated with respect to the ground state energy of **FM-190**.

14.4 kcal mol^{-1} and occurs by overcoming a very low energy barrier of 1.9 kcal mol^{-1}.

The acidity of aqua ligands coordinated to Pt was also estimated computationally. The first acidity constant was calculated for the deprotonation process of the mono-aquated Pt species, $[Pt^{IV}(N_3)(H_2O)(OH)_2(py)_2]^+$, generated in the first step as reported in Fig. 5. Starting from the bis-aquated Pt species, $[Pt^{IV}(H_2O)_2(OH)_2(py)_2]^{2+}$ the second investigated process involves the deprotonation of one water molecule coordinated to the Pt centre. As outlined previously, calculations failed to locate this species owing to the high acidity of the coordinated water molecule, which donates a proton to the released N_3^- ligand. Finally, the third acidity constant is relative to the deprotonation of the $[Pt^{IV}(H_2O)(OH)_3(py)_2]^+$ complex. The estimated values of the acidity constants obtained for the three processes illustrated above are:

$$[Pt^{IV}(N_3)(H_2O)(OH)_2(py)_2]^+ + H_2O \rightleftharpoons [Pt^{IV}(N_3)(OH)_3(py)_2] + H_3O^+ \quad K_a = 6.6 \times 10^{-6} \quad (1)$$

$$[Pt^{IV}(H_2O)_2(OH)_2(py)_2]^{2+} + H_2O \rightleftharpoons [Pt^{IV}(H_2O)(OH)_3(py)_2]^+ + H_3O^+ \quad K_a = 1.2 \times 10^{3} \quad (2)$$

$$[Pt^{IV}(H_2O)(OH)_3(py)_2]^+ + H_2O \rightleftharpoons [Pt^{IV}(OH)_4(py)_2] + H_3O^+ \quad K_a = 6.0 \times 10^{-7} \quad (3)$$

The large value of K_a for equation (2) means that the bis-aquated complex is a strong acid, and it dissociates completely as illustrated in Fig. 5, where it is shown that the formation of the $[Pt^{IV}(H_2O)_2(OH)_2(py)_2]^{2+}$ species and its deprotonation occur simultaneously.

2.5. Dark stability and photoactivation in plasma and PBS

Blood plasma and PBS were also used as media for the investigation of dark stability and photoactivation of **FM-190**. **FM-190** (7756 nM) in human plasma was incubated at 37 °C for 2 h in the dark, then transferred into a centrifugal filter unit (MWCO 5000) and centrifuged to remove proteins. The solvent was removed and the residue was redissolved in water to make a final 10× diluted solution. The major peak contains 97.7% of the total Pt eluting at *ca.* 14.2 min indicating the high dark stability of **FM-190** in human plasma (Fig. S11a†). For comparison, **FM-190** in PBS shows a similar retention time and a major peak Pt of 98.85% (Fig. S11b†). The sum of the Pt peak areas for the sample in plasma is about 95% of that in PBS, suggesting the high efficacy of this extraction method (Table S13†). Another extraction method that precipitates plasma proteins by addition of acetonitrile was also investigated. **FM-190** contributes 99.4% of the total Pt (Fig. S12a†). Although slightly larger peaks areas were observed by using this method, but the difference is within 5% (Tables S13 and S14†).

Photoproducts from **FM-190** (7756 nM) in plasma were also monitored by HPLC-ICP-MS after 1 h incubation at 37 °C in the dark and after 1 h irradiation (463 nm) at 25 °C, and then extracted using the same method as for the dark samples (Fig. S11c–d, S12b, Tables S14 and S15†). About 91% of **FM-190** undergoes photoactivation after irradiation. Compared to the photoproducts formed in water, plasma components might interact with those photoproducts, resulting in formation of many small peaks, while the number of the most intense peaks (peak area >10%) decreased to four. The extent of photoactivation in PBS is not as significant as that in plasma and the retention times of those photoproducts are different. Notably, the sum of peak areas determined for irradiated samples is about 12–36% lower than that for the corresponding dark samples.

LC-MS was carried out to identify the species formed by **FM-190** after irradiation (Fig. S13–S15†). Due to the complex matrix of plasma and the relatively low sensitivity of the LC-MS method, only the $[\{Pt^{IV}(py)_2(N_3)(OH)_3\} + Na]^+$ (*m*/*z* 468.96, **c**) peak was observed as the photoproduct of **FM-190** extracted using different protocols, even when a high concentration of 194.9 μM was used. Pt adducts might be formed with components of plasma, which are not detectable by LC-MS. For comparison, a number of smaller peaks other than *m*/*z* 468.96 were observed for samples in PBS due to its relatively simple matrix (Fig. S15†). Compared with the chromatogram obtained by HPLC-ICP-MS, there are some additional peaks in LC-MS attributable to plasma components, which form a complicated matrix.

3. Discussion

In contrast to labile square-planar d^8 Pt(II) complexes, low-spin d^6 Pt(IV) complexes are usually resistant to hydrolysis, but can undergo reduction in the presence of bio-reductants.[8] However, some combinations of ligands (*e.g.* axial carboxylates) can facilitate hydrolysis.[50–52] Identification and quantitative analysis of Pt metabolites *in vitro* and *in vivo* at bio-relevant concentrations is important for potential preclinical development of anticancer Pt drugs.[27,35,42,43]

HPLC-UV does not readily identify Pt species and does not allow a quantitative analysis due to the unknown extinction coefficients of each species. LC-MS gives structural information, but is not capable of quantitation owing to the different ionisation abilities among Pt species. Importantly, both detectors are not sensitive enough to detect Pt species at nanomolar concentrations. HPLC-ICP-MS with a high accuracy and sensitivity allows analysis of Pt metabolites extracted from cells and patients. The combination of LC-MS and HPLC-ICP-MS results provides accurate identification and quantitation of Pt samples, which provides a deeper insight into the metabolism of Pt anticancer drugs within biological systems.

Pt(IV) species were determined to be the main photoproducts when the activation light wavelength was 463 nm (blue light). Azide release from **FM-190** upon irradiation was observed at the same time as the replacement by hydroxido ligands, with $[\{Pt^{IV}(py)_2(N_3)(OH)_3\} + Na]^+$ (**c**) assigned by LC-MS as the main photoproduct (Fig. 1b). DFT calculations

suggest that it is favourable to form this species as the main product from the reaction between **FM-190** and water, directly in the singlet state. The large acidity constant K_a of $[Pt^{IV}(H_2O)_2(OH)_2(py)_2]^{2+}$ indicates that it is a strong acid which explains why $[\{Pt^{IV}(py)_2(N_3)(OH)_3\} + Na]^+$ is the main product. Despite DFT calculations indicating that Pt(II) species are the main photoproducts formed during photoactivation, we detected Pt(IV) species that require the overcoming of high energy barriers and unfavourable thermodynamics to be formed. In view of the high dark stability of **FM-190** in water, we assume that such reactions might be facilitated by the photoactivation. An alternative mechanism involving photoreduction, followed by ligand substitution on Pt(II) and re-oxidation by any strongly oxidising photoproducts formed seems less likely at low Pt concentrations.

Small amounts of Pt(II) species were also detected by LC-MS, but when the organic solvent ratio increased to 80%, they did not enter the ICP-MS detector. However, according to the difference between the total Pt peak areas of ICP-MS in dark and irradiated samples, these Pt(II) species make only an insignificant contribution to the total Pt after irradiation. The sum of ^{195}Pt peak areas in irradiated samples is even slightly higher (<10%) than that of the corresponding dark samples, which might be caused due to the slight difference in the detection sensitivity of ICP-MS detector for different Pt species. In contrast to irradiation at 463 nm, in the photoactivation of **FM-190** by indigo light (420 nm), Pt(II) species were determined to be the main photoproducts.[20] These results show that the products from photoactivation of **FM-190** with blue light (463 nm) gives more initial products than final products. DFT results also suggest the dissociative character of both azide ligands that can lead to the formation of the photoreduced Pt(II) species, $[Pt^{II}(OH)_2(py)_2]$. Therefore, photo-substituted Pt(IV) species can be assigned as the initial intermediates from the photoactivation of **FM-190** before photoreduction occurs. These are in agreement with a recent study on photosubstitution of **FM-190** as the first step of photoactivation using steady-state and laser flash photolysis.[53] However, no detailed structural information for photoproducts was reported using those methods. These results also indicate the

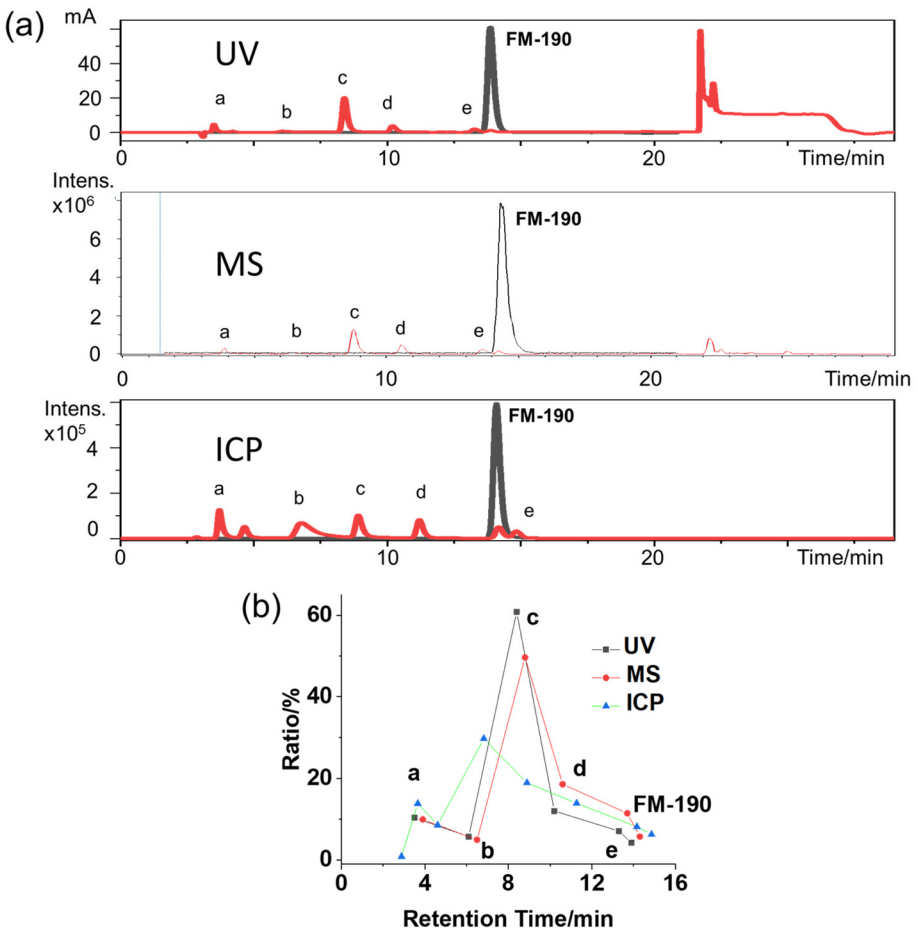

Fig. 6 (a) LC UV (detection wavelength 254 nm), MS and ICP-MS (^{195}Pt) signals of **FM-190** in MilliQ water obtained using method-7 for dark samples and method-8 for photoactivated samples (463 nm, 1 h). Species **a–e** are assigned in Table S5 (ESI†). (b) Ratio of Pt species with different retention times in irradiated samples determined using different detectors (assumes all species have same extinction coefficient and ionisation ability).

reason why +4 dominates the oxidization state of Pt in cellular accumulated **FM-190** in PC3 cancer cells after irradiation with blue light (465 nm).[54]

Using methanol rather than acetonitrile as the organic mobile phase did not affect the determination of Pt photoproducts, except for the retention time. Due to the different set-ups of the LC-MS and HPLC-ICP-MS, a small shift in retention times was observed. The parent compound **FM-190** served as a reference signal. The retention time of **FM-190** determined by UV, MS and ICP-MS under exactly the same conditions (method-7) was 13.9, 14.4 and 14.1 min, respectively (Fig. 6). In theory, a −0.3 min difference between MS and ICP-MS signals can be applied when assigning the Pt peaks detected by ICP. However, due to the different modes of detection, species **b–e** have a longer retention time in ICP-MS.

The three intense sharp ICP-MS Pt peaks **a**, **c** and **d** can be assigned as $[\{Pt^{IV}(py)_2(OH)_4\} + Na]^+$ (*m*/*z* 443.58, **a**); $[\{Pt^{IV}(py)_2(N_3)(OH)_3\} + Na]^+$ (*m*/*z* 468.58, **c**); and $[\{Pt^{III}(py)_2(HCOO)(OH)_2(H_2O)\} + Na]^+$ (*m*/*z* 472.57, **d**). Interestingly, only peak **c** shows an intense absorbance at 254 nm, attributable to its Pt–N_3 ligand-to-metal charge-transfer transition. In addition, the broad Pt peak **b** detected by ICP-MS gives very weak UV and MS signals. According to its MS isotopic pattern, this peak can be assigned to a dinuclear Pt species $[\{Pt^{IV}(py)_2(OH)_3\}_2(\mu\text{-}O_2) + Na]^+$ (*m*/*z* 863.04, **b**), which might explain its intense ICP signal. Due to the high sensitivity of ICP-MS detection mode, analysis of Pt photoproducts at biologically relevant concentrations (low nM levels) only becomes feasible with LC-MS analysis using a higher **FM-190** concentration (double-digit μM). Based on these results, a potential photoactivation pathway for **FM-190** in aqueous solution with visible light irradiation can be proposed, as shown in Fig. S16.†

An interesting observation is the effect of the concentration of the compound on the number of peaks detected, not only by ICP-MS, but also UV and MS. At low concentrations, photoactivation of **FM-190** is less likely to lead to intermolecular interactions in the formation of products compared to high concentrations. Another reason for the missing Pt peaks is their low concentrations, below the detection limit of the method.

The extraction of Pt drugs and their photo-products from biofluids, such as blood plasma, is an essential step in drug development. Two methods, centrifugal filter unit (MWCO 5000) centrifugation and acetonitrile precipitation, were employed to precipitate proteins in plasma to give Pt-containing solutions suitable for HPLC separation. Both methods gave a high recovery for Pt species, with a difference <5% compared to the same samples in PBS. Notably, the sum of peak areas determined for irradiated samples is about 12–36% lower than that for the corresponding dark samples. No Pt species were detectable in plasma samples when the organic mobile phase was increased to 80% for LC-MS. These results indicate that adducts between photoproducts and plasma are either insoluble in water or have a molecular weight >5000 Da.[42] Considering the complex matrix of low and high molecular-weight components in plasma, a range of species was detected by LC-MS which complicated the analysis. This problem was simplified using HPLC-ICP-MS, which gives signals only for Pt species.

4. Conclusions

Photoactive Pt(IV) complexes are promising next-generation platinum anticancer drugs due to their high photo-selectivity and novel mechanisms of action. Investigations of photoproducts from diazido Pt(IV) complexes in cells and tissues plays an important role in the exploration of their mechanism of action. In this work, an analytical speciation approach for **FM-190** and its photoproducts has been developed using HR-MS, LC-MS and HPLC-ICP-MS. LC-MS and HR-MS were employed to identify these photoproducts. Interestingly $[\{Pt^{IV}(py)_2(N_3)(OH)_3\} + Na]^+$ and $[\{Pt^{IV}(py)_2(OH)_4\} + Na]^+$ resulting from the replacement of azide by hydroxide were detected by MS and characterised, with $[\{Pt^{IV}(py)_2(N_3)(OH)_3\} + Na]^+$ as the most abundant photoproduct.

Our findings highlight the need to investigate further the chemical and biological activity of tri- and tetra-hydroxido Pt(IV) complexes, and their possible role in the photocytotoxicity, where very little knowledge is currently available. The DFT calculations estimate that the first pK_a values for these complexes are close to the pH values in the cell cytoplasm and various organelles (*ca.* 5.6–7.4). It might be expected that a coordinated aqua ligand will be much more reactive towards substitution than a hydroxido ligand. Also axial hydroxido ligands on Pt(IV) tend to stabilise Pt(IV) towards reduction, although the introduction of cis-hydroxido ligands may give rise to new reaction pathways. Studies of the electrochemical properties of such complexes might help to elucidate this.

It will also be interesting to investigate possible adducts of these hydroxide complexes with biological macromolecules such as proteins and oligonucleotides. Depending on the specific geometrical arrangement of the hydroxido ligands (which also needs to be investigated), these tri-and tetra-hydroxido Pt(IV) complexes offer strong H-bond donor and acceptor sites.

By combining the results from LC-MS and HPLC-ICP-MS, species at nanomolar concentration can be separated and assigned to analyse potential photodecomposition pathways for Pt(IV) complexes, which is essential for elucidation of the mechanism of photoactivation for these prodrugs. Both ultrafiltration and protein precipitation methods proved useful for analysis of low molecular-weight Pt species arising from **FM-190**.

FM-190 displays extremely high stability in human plasma in the dark at 37 °C, with promising ability to undergo photoactivation when exposed to blue light (463 nm). Work is in progress on other related diazido Pt(IV) complexes in this family which can be activated by longer wavelengths of light and penetrate more deeply into tissues. The high separation power of HPLC combined with the high detection capability of

ICP-MS provide an important strategy for the speciation analysis of photoactive Pt(IV) complexes and their photoproducts with biomolecules in cells and tissues, such analysis is important for the investigation of the stability and metabolism of platinum drugs *in vivo*. In future work HPLC-ICP-MS methods which allow higher ratios of organic solvent will be developed to allow exploration of lipophilic photoactive Pt(IV) complexes, for which **FM-190** can be used as an internal standard.

Author contributions

H. S., C. W.-D., P. J. S. and H. G.-I. designed the experiments, H. S. and C. W.-D. carried out HPLC-ICP-MS experiments, H. S. also carried out LC-MS and HR-MS experiments. F. P. and E. S. carried out DFT and TDDFT calculations. All authors drafted the script and contributed to the final submission.

Data availability

The data supporting this article have been included as part of the ESI.†

Conflicts of interest

There are no conflicts to declare.

Acknowledgements

We thank the Engineering and Physical Sciences Research Council (EPSRC Grant No. EP/P030572/1), Anglo-American Platinum (fellowship for H. S.), the Italian Association for Cancer Research, AIRC (ID 25578 for F. P.), University of Calabria, and Department of Science Innovation and Technology (DSIT) for funding. We thank Dr Lijiang Song for assistance with HR-MS.

References

1 S. Ghosh, *Bioorg. Chem.*, 2019, **88**, 102925.
2 C. Zhang, C. Xu, X. Gao and Q. Yao, *Theranostics*, 2022, **12**, 2115–2132.
3 S. Rottenberg, C. Disler and P. Perego, *Nat. Rev. Cancer*, 2021, **21**, 37–50.
4 K. Peng, B. B. Liang, W. Liu and Z. W. Mao, *Coord. Chem. Rev.*, 2021, **449**, 214210.
5 H. Shi, C. Imberti and P. J. Sadler, *Inorg. Chem. Front.*, 2019, **6**, 1623–1638.
6 H. Shi and P. J. Sadler, *Adv. Inorg. Chem.*, 2022, **80**, 95–127.
7 L. Qi, Q. Luo, Y. Zhang, F. Jia, Y. Zhao and F. Wang, *Chem. Res. Toxicol.*, 2019, **32**, 1469–1486.
8 Z. Xu, Z. Wang, Z. Deng and G. Zhu, *Coord. Chem. Rev.*, 2021, **442**, 213991.
9 Z. Deng and G. Zhu, *Curr. Opin. Chem. Biol.*, 2023, **74**, 102303.
10 J. Gurruchaga-Pereda, Á. Martínez, A. Terenzi and L. Salassa, *Inorg. Chim. Acta*, 2019, **495**, 118981.
11 J. Huang, W. Ding, X. Zhu, B. Li, F. Zeng, K. Wu, X. Wu and F. Wang, *Front. Chem.*, 2022, **10**, 876410.
12 M. Imran, W. Ayub, I. S. Butler and Zia-ur-Rehman, *Coord. Chem. Rev.*, 2018, **376**, 405–429.
13 D. Spector, K. Pavlov, E. Beloglazkina and O. Krasnovskaya, *Int. J. Mol. Sci.*, 2022, **23**, 14511.
14 P. Müller, B. Schröder, J. A. Parkinson, N. A. Kratochwil, R. A. Coxall, A. Parkin, S. Parsons and P. J. Sadler, *Angew. Chem., Int. Ed.*, 2003, **42**, 335–339.
15 F. S. Mackay, J. A. Woods, H. Moseley, J. Ferguson, A. Dawson, S. Parsons and P. J. Sadler, *Chem. – Eur. J.*, 2006, **12**, 3155–3161.
16 L. Ronconi and P. J. Sadler, *Dalton Trans.*, 2011, **40**, 262–268.
17 L. Ronconi, A. M. Pizarro, R. J. McQuitty and P. J. Sadler, *Chem. – Eur. J.*, 2011, **17**, 12051–12058.
18 F. S. Mackay, J. A. Woods, P. Heringova, J. Kašpárková, A. M. Pizarro, S. A. Moggach, S. Parsons, V. Brabec and P. J. Sadler, *Proc. Natl. Acad. Sci. U. S. A.*, 2007, **104**, 20743–20748.
19 N. J. Farrer, J. A. Woods, L. Salassa, Y. Zhao, K. S. Robinson, G. Clarkson, F. S. MacKay and P. J. Sadler, *Angew. Chem., Int. Ed.*, 2010, **49**, 8905–8908.
20 R. R. Vernooij, T. Joshi, M. D. Horbury, B. Graham, E. I. Izgorodina, V. G. Stavros, P. J. Sadler, L. Spiccia and B. R. Wood, *Chem. – Eur. J.*, 2018, **24**, 5790–5803.
21 N. S. Ha, M. de Raad, L. Z. Han, A. Golini, C. J. Petzold and T. R. Northen, *RSC Chem. Biol.*, 2021, **2**, 1331–1351.
22 M. Kandiah and P. L. Urban, *Chem. Soc. Rev.*, 2013, **42**, 5299–5322.
23 X. Huang, H. Liu, D. Lu, Y. Lin, J. Liu, Q. Liu, Z. Nie and G. Jiang, *Chem. Soc. Rev.*, 2021, **50**, 5243–5280.
24 J. Feldmann, A. Raab and E. M. Krupp, *Anal. Bioanal. Chem.*, 2018, **410**, 661–667.
25 S. C. Wilschefski and M. R. Baxter, *Clin. Biochem. Rev.*, 2019, **40**, 115–133.
26 A. R. Timerbaev, *J. Anal. At. Spectrom.*, 2021, **36**, 254–266.
27 M. Patriarca, N. Barlow, A. Cross, S. Hill, A. Robson, A. Taylor and J. Tyson, *J. Anal. At. Spectrom.*, 2022, **37**, 410–473.
28 J. G. Dorsey and K. A. Dill, *Chem. Rev.*, 1989, **89**, 331–346.
29 P. Žuvela, M. Skoczylas, J. J. Liu, T. Bączek, R. Kaliszan, M. W. Wong and B. Buszewski, *Chem. Rev.*, 2019, **119**, 3674–3729.
30 H. R. Hansen and S. A. Pergantis, *J. Anal. At. Spectrom.*, 2006, **21**, 1240–1248.
31 X. Yan, Y. Zhou, H. Li, G. Jiang and H. Sun, *Ref. Modul. Chem. Mol. Sci. Chem. Eng.*, 2023, 53–76.
32 Y. Zhou, H. Li and H. Sun, *Annu. Rev. Biochem.*, 2022, **91**, 449–473.
33 M. Montes-Bayón, K. DeNicola and J. A. Caruso, *J. Chromatogr. A*, 2003, **1000**, 457–476.
34 D. P. Bishop, D. J. Hare, D. Clases and P. A. Doble, *Trends Anal. Chem.*, 2018, **104**, 11–21.

35 A. R. Timerbaev, *J. Anal. At. Spectrom.*, 2014, **29**, 1058–1072.
36 L. H. Møller, C. S. Jensen, T. T. T. N. Nguyen, S. Stürup and B. Gammelgaard, *J. Anal. At. Spectrom.*, 2015, **30**, 277–284.
37 G. Hermann, P. Heffeter, T. Falta, W. Berger, S. Hann and G. Koellensperger, *Metallomics*, 2013, **5**, 636–647.
38 Z. Yao, B. Li, C. Li, B. Wang, M. Zhao and Z. Ma, *J. Anal. At. Spectrom.*, 2022, **37**, 1652–1657.
39 J. Wang, J. Tao, S. Jia, M. Wang, H. Jiang and Z. Du, *Pharmaceuticals*, 2021, **14**, 104.
40 G. A. Zachariadis and O. E. Misopoulou, *Anal. Lett.*, 2018, **51**, 1060–1070.
41 L. Galvez, M. Rusz, M. A. Jakupec and G. Koellensperger, *J. Anal. At. Spectrom.*, 2019, **34**, 1279–1286.
42 R. Larios, M. E. Del Castillo Busto, D. Garcia-Sar, C. Ward-Deitrich and H. Goenaga-Infante, *J. Anal. At. Spectrom.*, 2019, **34**, 729–740.
43 S. Cuello-Nuñez, R. Larios, C. Deitrich, T. Lekishvili, V. Nischwitz, B. L. Sharp and H. Goenaga-Infante, *J. Anal. At. Spectrom.*, 2017, **32**, 1320–1330.
44 A. Martinčič, M. Cemazar, G. Sersa, V. Kovač, R. Milačič and J. Ščančar, *Talanta*, 2013, **116**, 141–148.
45 B. Michalke, *J. Trace Elem. Med. Biol.*, 2010, **24**, 69–77.
46 M. A. El-Sayed, *J. Chem. Phys.*, 1963, **38**, 2834–2838.
47 D. Escudero, E. Heuser, R. J. Meier, M. Schäferling, W. Thiel and E. Holder, *Chem. – Eur. J.*, 2013, **19**, 15639–15644.
48 D. Escudero and W. Thiel, *J. Chem. Phys.*, 2014, **140**, 194105.
49 Y. Zhang, Z. Guo and X. Z. You, *J. Am. Chem. Soc.*, 2001, **123**, 9378–9387.
50 A. Kastner, I. Poetsch, J. Mayr, J. V. Burda, A. Roller, P. Heffeter, B. K. Keppler and C. R. Kowol, *Angew. Chem., Int. Ed.*, 2019, **58**, 7464–7469.
51 I. Ritacco, G. Mazzone, N. Russo and E. Sicilia, *Inorg. Chem.*, 2016, **55**, 1580–1586.
52 J. Zhao, Z. Xu, J. Lin and S. Gou, *Inorg. Chem.*, 2017, **56**, 9851–9859.
53 G. I. Zhdankin, V. P. Grivin, V. F. Plyusnin, P. A. Tkachenko, D. B. Vasilchenko and E. M. Glebov, *Mendeleev Commun.*, 2023, **33**, 61–63.
54 E. M. Bolitho, C. Sanchez-Cano, H. Shi, P. D. Quinn, M. Harkiolaki, C. Imberti and P. J. Sadler, *J. Am. Chem. Soc.*, 2021, **143**, 20224–20240.